CLIMATOLOGY

A multiyear tropical Pacific cooling response to recent Australian wildfires in CESM2

John T. Fasullo*, Nan Rosenbloom, Rebecca Buchholz

The climate response to biomass burning emissions from the 2019–2020 Australian wildfire season is estimated from two 30-member ensembles using CESM2: one of which incorporates observed wildfire emissions and one that does not. In response to the fires, an increase in biomass aerosol burdens across the southern hemisphere is simulated through late 2019 and early 2020, accompanied by an enhancement of cloud albedo, particularly in the southeastern subtropical Pacific Ocean. In turn, the surface cools, the boundary layer dries, and the moist static energy of the low-level flow into the equatorial Pacific is reduced. In response, the intertropical convergence zone migrates northward and sea surface temperature in the Niño3.4 region cools, with coupled feedbacks amplifying the cooling. A subsequent multiyear ensemble mean cooling of the tropical Pacific is simulated through the end of 2021, suggesting an important contribution to the 2020–2022 strong La Niña events.

INTRODUCTION

The 2019–2020 Australian wildfire season was exceptional in both its severity and particulate emissions, driving the maximum in observed aerosol optical depth in the southern hemisphere over recent decades (*1*–*3*). Coupled simulations of its climate impact also show responses in clouds and radiation on a planetary scale, similar to those simulated for a major volcanic eruption, suggesting the potential for a broad range of climate responses (*4*). In this work, we explore the influence of these wildfires on sea surface temperature (SST) in the tropical Pacific Ocean and analyze the mechanisms connecting the two.

The El Niño–Southern Oscillation (ENSO) is a highly coupled mode of internal variability that affects climate worldwide and involves interactions between the ocean, atmosphere, and land surface (*5*). While the mode is fundamentally one that is internal to the climate system, external forcing has been shown to influence both its occurrence and character (*6*, *7*). One such influence that has been widely explored in climate models is the response of ENSO to major volcanic eruptions (*8*, *9*). The response is characterized by the emergence of La Niña conditions in the year following major eruptions in the southern hemisphere and is associated with northward displacement of the intertropical convergence zone (ITCZ) due to the imposed interhemispheric gradient in the atmospheric energy budget (*8*–*12*). Questions therefore arise as to whether the energetic imbalance driven by the Australian wildfires is capable of exacting a similar response in the ITCZ and what the associated implications are for ENSO and tropical SST generally. The mechanisms that may connect the fires to equatorial Pacific Ocean SST are also uncertain. The importance of these questions is underscored further by the emergence of cool tropical Pacific SSTs following the 2019–2020 wildfire season and persisting through 2022, and the ongoing uncertainty surrounding their origin.

In this work, these questions are explored in a pair of initialized coupled climate model ensembles spanning several years using the Community Climate System Model version 2 (CESM2), one in which climatological fire emissions are prescribed globally, referred to as the "control" ensemble, and one in which satellite retrieved estimates of the 2019–2020 Australian wildfire emissions are used, referred to as the "AF" ensemble (see Materials and Methods) (*13*). CESM2 explicitly represents interactions between biomass aerosols and clouds, including the effects of aerosol aging, making it well suited for assessing the fires' climate effects. Like most climate models, it does not, however, include a plume model for estimating the vertical distribution of aerosols, leading to a possible underestimation of climate effects (see Results). Each ensemble consists of 30 members, initialized from highly similar, though not identical, atmospheric initial states within each ensemble (*14*). Corresponding members between the two ensembles use identical initial states, and there is therefore no initial state influence on the ensemble mean difference, which serves as an estimate of the climate system response to the Australian wildfires and hereafter is referred to simply as the wildfire response. The initialized ensembles have the benefit over free-running coupled simulations, such as those used in recent work, in that the spread in their initial conditions is extremely small and resembles the physical state occurring in nature (*4*). The associated reduction in ensemble spread relative to uninitialized ensembles is detectable for well over a year (fig. S1). As a result, the ensembles used here allow for a more precise estimation of the climate wildfire response than the uninitialized ensembles used in prior work (*4*). The ensembles depict a response characterized by a multiyear cooling of the tropical Pacific Ocean and a sequence of events that connects the wildfire emissions to the cooling through their influence on (i) subtropical clouds and radiation, (ii) boundary layer moist static energy (MSE) and ocean mixed layer temperature, and (iii) the advection of these influences into the equatorial Pacific Ocean (5°N to 5°S).

RESULTS

Large-scale climate responses

Emissions from fires include a broad range of aerosol species and aerosol precursors. The associated atmospheric aerosol burdens can play an important role in influencing Earth's energy budget, both by directly scattering and absorbing radiation and by indirectly influencing cloud properties through microphysical interactions.

National Center for Atmospheric Research, Boulder, CO 80305, USA.
*Corresponding author. Email: fasullo@ucar.edu

Primary organic matter (POM) burdens are a key contributor to the aerosol mass and are used here as a useful indicator of the broader aerosol effects of the fires. The 2019–2020 Australian fires drove a notable increase in POM burdens in CESM2 on a planetary scale, with a quadrupling of burdens from 30°S to 60°S in late 2019 from their climatological annual maximum values (Fig. 1). The seasonality of Australian fires and fire emissions averaged over all of Australia generally follows the pattern of northwest Australia, which peaks between August to October (*15*). The southeast region fire season typically peaks in December and January, but usually does not burn as extremely as in 2019–2020, and thus, the key in 2019–2020 was the extremely intense fires and increased emissions from the southeast. The increases occurred at a time of year in which atmospheric burdens are typically in decline (Fig. 1A, gray line). Advected by strong southern hemisphere zonal winds, the emissions were of sufficient quantity to encircle the globe in about a month. Maxima in southern hemisphere aerosol optical depth and direct radiative effects occurred in late 2019 and were sustained into early 2020 (Fig. 1B). The timing of the burden maximum agrees closely with that observed from satellite, although its magnitude is underestimated in our ensemble based on comparison against satellite retrievals of aerosol optical depth (figs. S2 and S3). This underestimation of aerosol burdens in CESM2 is also consistent with prior work that more generally evaluates organic aerosol burdens in CESM2 using satellite and aircraft observations (*16*). In this context, the climate response in CESM2 to the fires may be a conservative estimate of the response in nature, depending on the role played by other uncertain processes (see Discussion).

The seasonal timing of the peak in aerosol burdens is noteworthy in that it coincides with the southern hemisphere summer solstice and therefore with the annual maximum in solar insolation. The ensemble mean simulation differences depict an anomalous interhemispheric radiative gradient driven by the burdens that reaches a peak of about 3 W m^{-2} at the end of 2019 (Fig. 1C). The interhemispheric radiative perturbation is driven mainly by anomalous southern hemisphere albedo, which, when scaled by the solstice's strong solar insolation, results in an approximately 3 W m^{-2} reduction in absorbed shortwave radiation that is in phase with aerosol burdens. In contrast, anomalies in longwave radiation are not detectable from noise across the simulation period (Fig. 1D, thin line) and therefore do not feature prominently in the fire's large-scale energetic effects. The clear-sky flux anomalies in both the

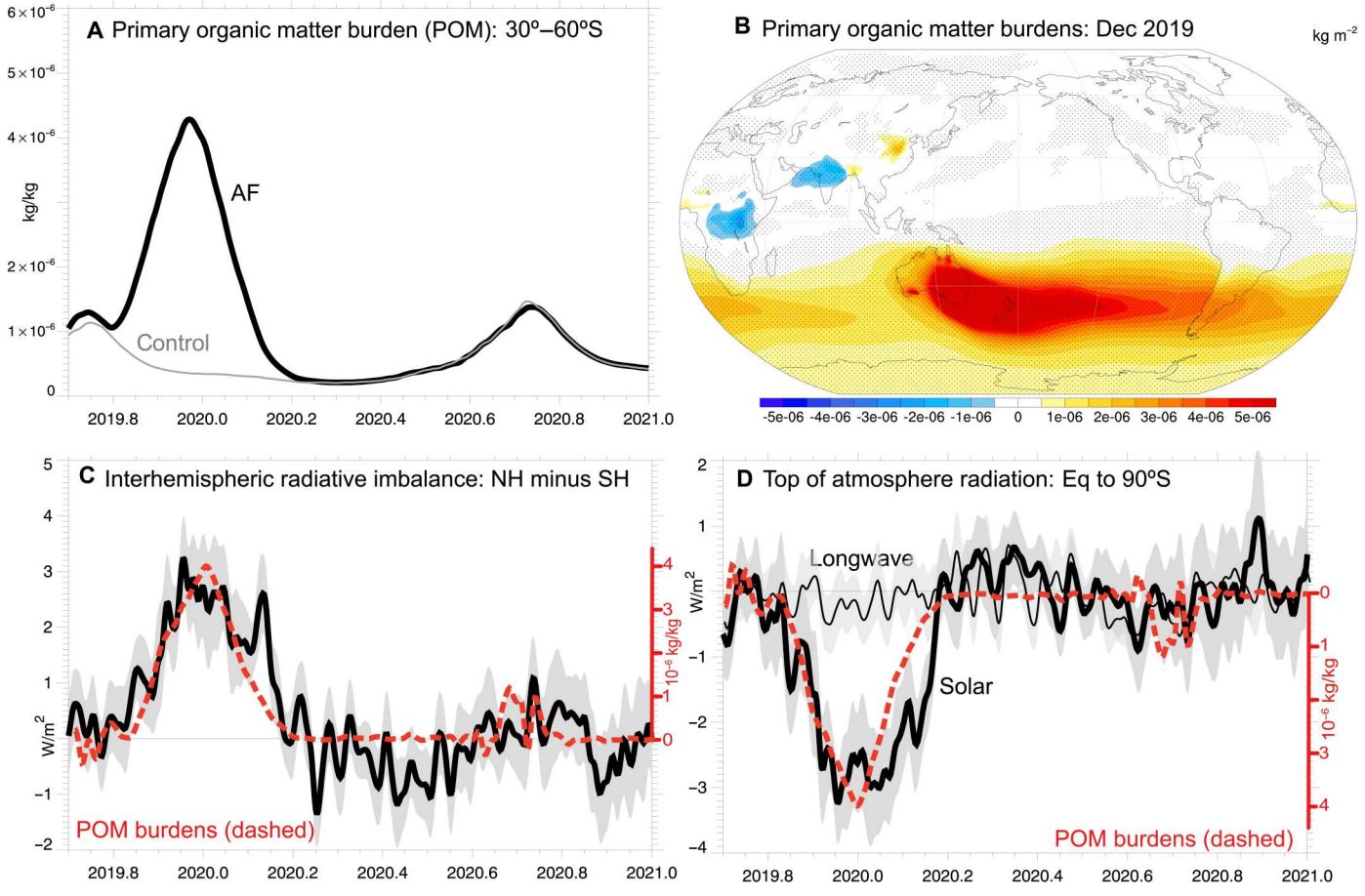

Fig. 1. Large-scale climate responses. The ensemble mean evolution of POM burdens from 30°S to 60°S (**A**) in control and AF (gray) and the spatial distribution of their differences in December 2019 (**B**). Associated responses in the interhemispheric radiative imbalance anomaly (**C**) and southern hemisphere (SH) top of atmosphere radiation (**D**) (solar, thick; longwave, thin) are also shown. Responses in POM burdens (dashed), defined as the difference between lines in (A), are scaled to match the target data and overlain in (C) and (D) to illustrate their in-phase relationship. Shading corresponds to twice the ensemble standard error. Stippling is shown in (B) where anomalies exceed twice the ensemble standard error.

shortwave and longwave fields are small generally relative to the all-sky anomalies, highlighting a central role for clouds (*4*). A resultant cooling response of the southern hemisphere of about 0.09 ± 0.03 K in early 2020 is simulated. Notably, the large-scale climate responses, which are less sensitive to internal variability than the regional features that we focus on below, agree closely between the initialized ensemble used here and the uninitialized ensembles used in prior work (*4*).

Responses in the tropical Pacific

Cooling in the Niño3.4 region is simulated in both the AF and control ensembles as shown in Fig. 2A, where background drift has been removed (see Materials and Methods), suggesting that a component of the simulated cooling results from the initial state (*14*). By focusing on differences between the ensembles in subsequent analysis, the effects of this initial condition cooling are removed. There is little detectable influence of biomass burning emissions by late 2019, as both ensembles cool by about 0.65 K and the ensemble ranges (Fig. 2A, whiskers) overlap. Beginning in early 2020, the ensembles begin to diverge, with additional cooling of about 0.2 K by June 2020 in the AF ensemble, a time at which ensemble differences also begin to emerge from noise as the ensemble ranges do not overlap. The inter-ensemble difference in cooling grows through late 2020, when it is about 0.4 K in magnitude, before decreasing to about 0.3 K in mid-2021. The cooling response is statistically significant as the ensemble ranges are largely distinct. The cooling response extends into late 2021 and is discussed in further detail below. The spatial pattern of the cooling response is shown in Fig. 2B for October 2020 and Fig. 2C for October 2021. Statistically detectable cooling in 2020 is located mainly in the eastern tropical and subtropical southeastern Pacific Ocean, where responses of about 0.5 K are simulated and ensemble ranges are again distinct (stippling). A cooling response across the entirety of the tropical Pacific is depicted in the inter-ensemble differences, although statistical robustness is limited to regions east of the dateline. In October 2021, a statistically robust cooling persists, although at this time anomalies are strongest in the central Pacific Ocean, with detectable responses centered near the dateline. While a robust and persistent cooling response in the tropical Pacific Ocean is simulated, a key outstanding question relates to the mechanisms that connect it to the Australian wildfire's emissions and this will be the focus of the sections below.

Responses of clouds, albedo, and radiation in the southeastern subtropical Pacific

While aerosols from the Australian wildfires are simulated to be advected throughout the southern hemisphere (Fig. 1A), their radiative effects have strong regional and temporal structure. In part, this structure is influenced by the cloud distribution, with particularly strong responses in the stratocumulus cloud decks that reside in the eastern subtropical ocean basins. Due in part to the confluence of large aerosol burdens that drive strong increases in cloud condensation nuclei in the lower troposphere (fig. S3), with its particularly expansive cloud decks, the southeastern subtropical Pacific (SESP) Ocean is the region with the greatest albedo sensitivity to Australian wildfire emissions (Fig. 3), with a reduction in surface downwelling solar radiation of about 15 W m^{-2} over an expanse of about 10^{13} m^2 (Fig. 3A). The radiation anomalies coincide in both space and time with elevated burden-driven changes in cloud albedo (Fig. 3B) and liquid water path (Fig. 3C), consistent with cloud microphysical effects represented in CESM2 (see Materials and Methods). Following the changes in clouds and radiation, the surface cools and boundary layer specific humidity decreases in the region (Fig. 3, D and E).

The in-phase relationship between POM burdens and cloud properties, and the lagging relationship with humidity and temperature, is suggestive of causal connections between these fields. Suggested effects include an in-phase brightening and thickening of the cloud field by aerosols through rapid microphysical interactions, an associated rapid reduction of solar radiation reaching the surface due to cloud changes, and a lagged reduction of surface temperature and near-surface specific humidity in response to radiation anomalies. An outstanding question is whether the anomalies in the SESP region have the capacity to influence the tropical Pacific Ocean, and if so, how.

Responses in the equatorial Pacific occur after the reductions of temperature, humidity, and MSE in the SESP region, and these responses remain largely detectable through late 2021. By May 2020, the wildfire response in the equatorial Pacific is characterized by a northward displacement of the ITCZ, with an anomalously strong band of precipitation at 10°N and weak precipitation in the equatorial Pacific (Fig. 4A). As denoted by the mean near-surface wind field (Fig. 4A), the SESP region lies directly upstream of the deep tropical Pacific, emphasizing potential connections between the regions via advection. Anomalies in the circulation also contribute to additional low-level advection in early 2020 (fig. S4). A sequence of events in the months before May 2020 suggests an important coupling between the response in the SESP region and tropical Pacific Ocean precipitation (fig. S4). Shortly after the peak cooling in the SESP region, reductions in MSE in the equatorial Pacific are simulated (Fig. 3B). The reductions coincide with decreases in specific humidity (Fig. 3C) and are associated with a northward migration and zonal broadening of the humidity reductions originating in the SESP region, consistent with their advection by the low-level wind field (fig. S5). The spatial structure and temporal evolution of the humidity response are also suggestive of having a causal role in driving a northward ITCZ displacement (fig. S4), as reductions in precipitation occur coincident with the arrival of decreased boundary layer specific humidity (Fig. 3C and fig. S5). At the time of ITCZ displacement, surface temperature in the equatorial Pacific also drops abruptly (Fig. 3E) and the cooling response persists through the end of 2021 (note the extended time scale in Fig. 4E). The spatial structure of cooling is initially greatest in the SESP region (March 2020; fig. S6B), expanding through May 2020, as these anomalies are advected northward across the equator and eastward across the dateline (fig. S6). Associated transects of ocean temperature anomalies in the equatorial Pacific from January 2020 to January 2021 are shown in fig. S7. Once the SST anomalies in the SESP extend into the equatorial Pacific, dynamical feedbacks associated with La Niña likely play an important role in the strengthening of cool anomalies in ensuing months. As shown in Fig. 2, the spatial structure is mainly characterized by strong cooling in the eastern equatorial Pacific in October 2020, which extends increasingly into the central and eastern Pacific Ocean by October 2021.

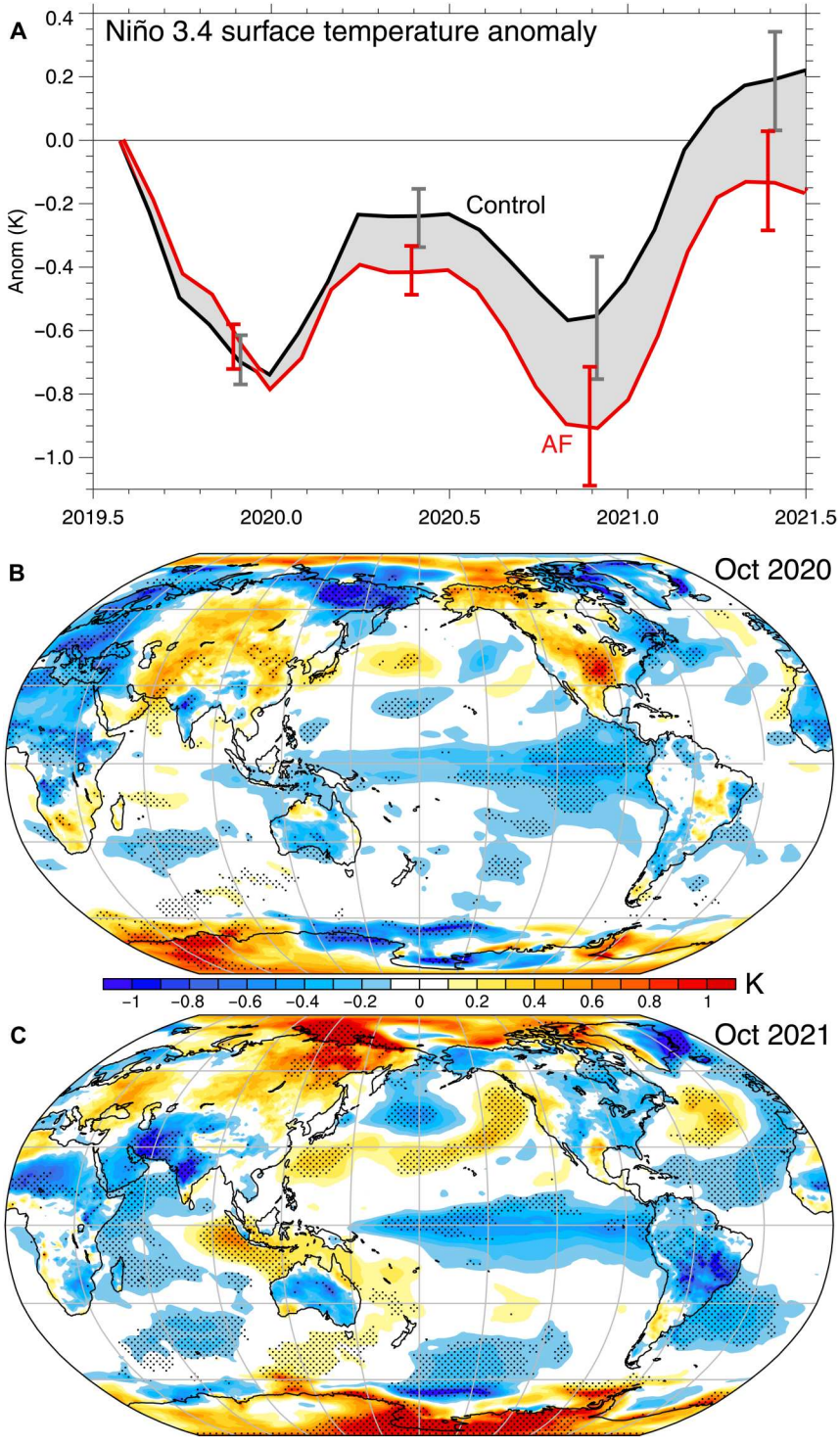

Fig. 2. Responses in the tropical Pacific Ocean. (**A**) The ensemble mean control (black) and AF (red) projections are shown for SST anomalies in the Niño3.4 region over the period for which drift correction is available (see Materials and Methods). Maps of the spatial structure of differences in surface temperature are also shown for (**B**) October 2020 and (**C**) October 2021, illustrating the persistent cooling of the tropical Pacific in the AF ensemble relative to the control ensemble. Regions where ensemble differences exceed twice the ensemble standard error are stippled.

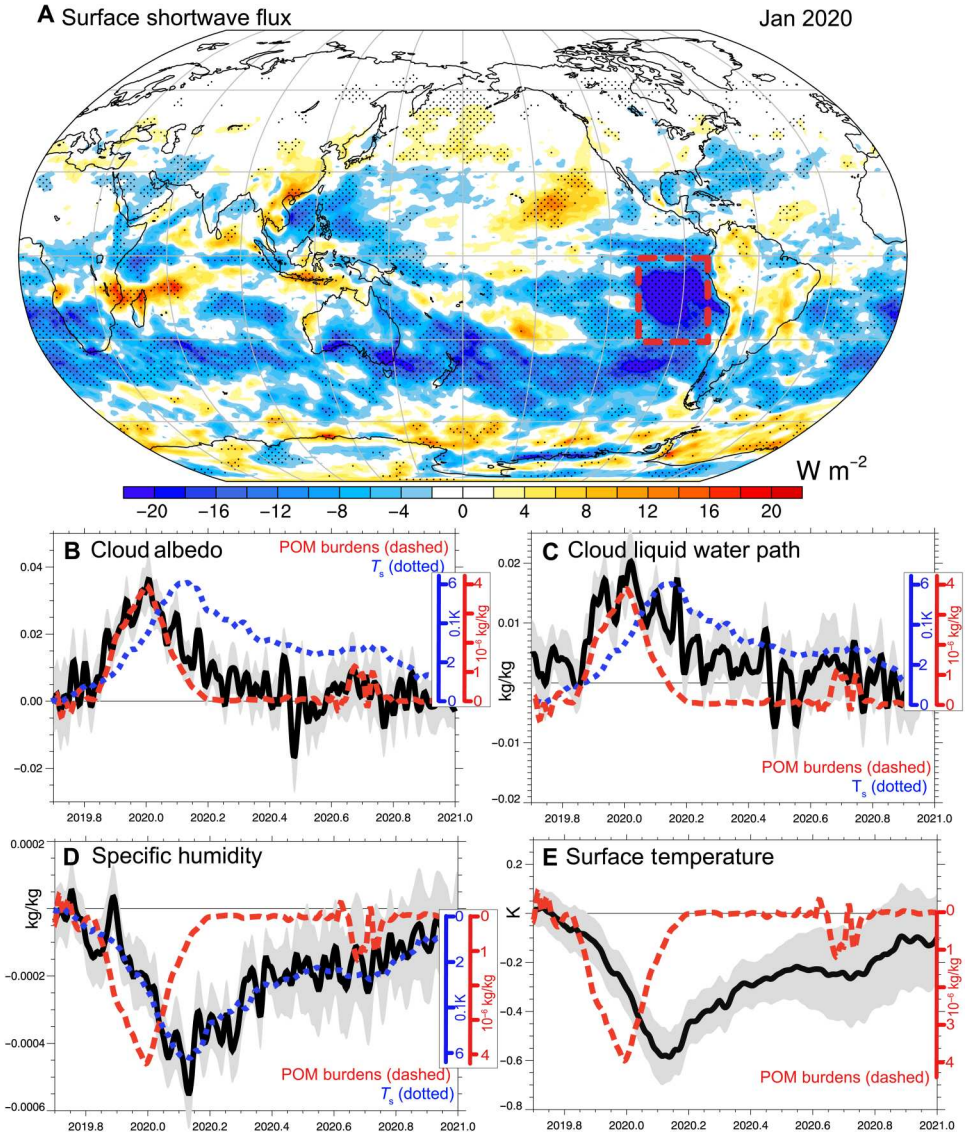

Fig. 3. Responses in the SESP Ocean. (**A**) Ensemble mean difference in surface downwelling shortwave radiation between the AF and control ensembles, stippled where differences exceed twice the ensemble standard error. The SESP region is outlined [red dashed lines in (A)]. The response in the SESP region of cloud albedo (**B**), cloud liquid water path (**C**), 2-m specific humidity (**D**), and SST (**E**) is also shown. Responses in POM burdens (Fig. 1, red dashed) and surface temperature (T_S) in the SESP region (E) are scaled to match the target data and overlain to illustrate their relative phase.

DISCUSSION

Using targeted 30-member initialized ensembles from CESM2, this work identifies responses in the subtropical and tropical Pacific Ocean to emissions from the 2019–2020 Australian wildfire season. A strong response in the SESP region is found to be driven by anomalous aerosol burdens and their influence on cloud properties, radiation, ocean temperature, and boundary layer MSE. Connections between the SESP region and the tropics, via both atmospheric and oceanic advection, are also inferred from atmospheric (figs. S4 and S5) and oceanic (fig. S6) near-surface circulations. Associated responses in the equatorial Pacific include surface cooling, reductions in near-surface specific humidity and MSE, and a northward displacement of the ITCZ. A number of associated responses, such as in the Walker circulation, in the strength and propagation of intraseasonal disturbances, and in the strength and temperature of ocean currents, are likely given their known sensitivity to the fields examined here, and these have the capacity to contribute to additional equatorial cooling (*16*, *17*). It is not possible, however, from the simulations used in this analysis, to estimate the relevant importance of these various influences, and this is therefore left for follow-on work. Such investigations are likely to be complementary to ongoing efforts to understand the detailed mechanisms governing responses to volcanic eruptions (*18*).

The analysis provides context for the recent La Niña event beginning in late 2020, which was unusual in many respects (*17*). Most notably, it did not follow a major El Niño event, with weak SST anomalies existing in early 2020, and therefore was not accompanied several months in advance by reflected upwelling Kelvin

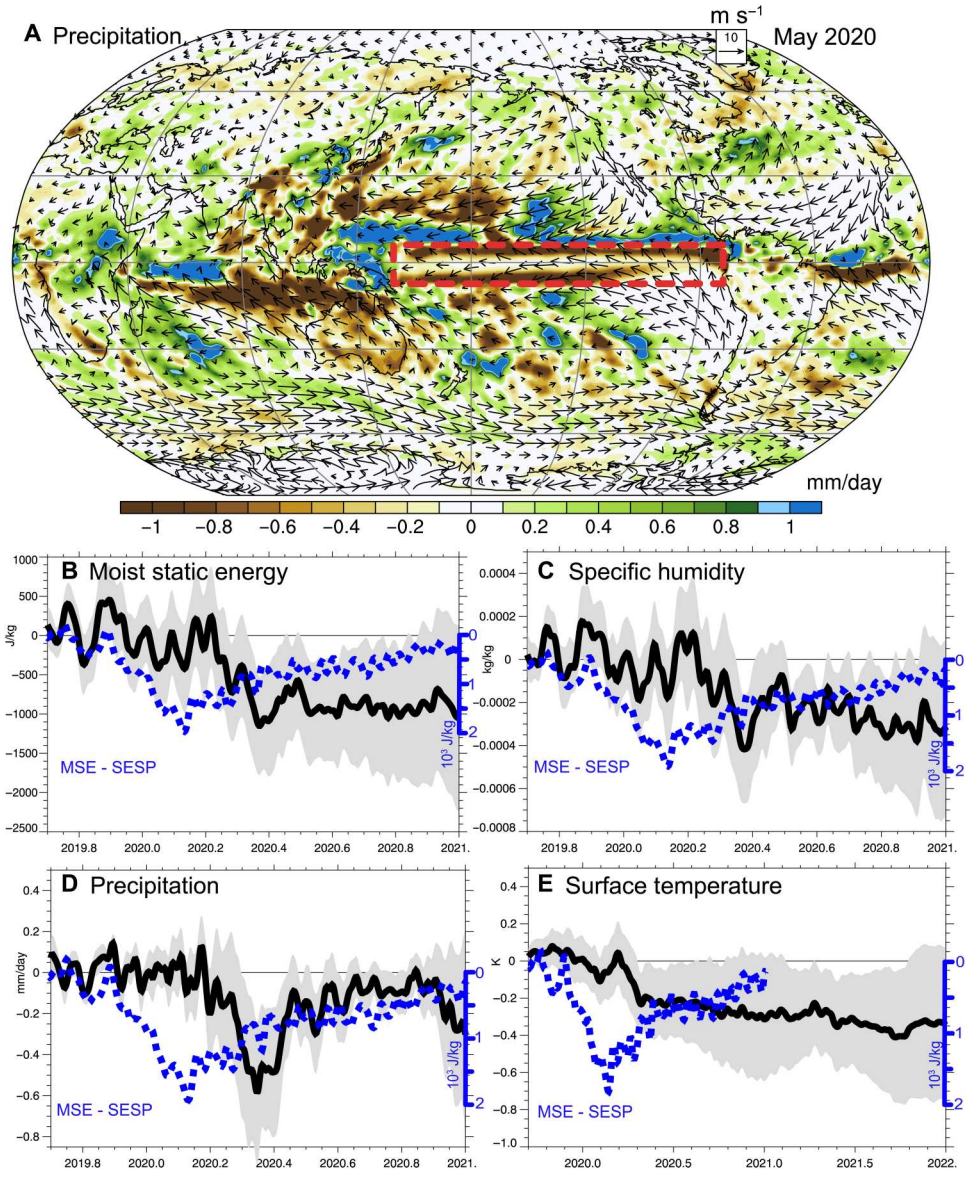

Fig. 4. Evolution of responses in the equatorial Pacific Ocean. (**A**) Response in precipitation in May 2020. The mean near-surface wind field in the AF ensemble is also shown (vectors, m s^{-1}) to illustrate advection from the SESP region to the equatorial Pacific Ocean. The temporal evolutions of 2-m MSE (**B**), 2-m specific humidity (**C**), precipitation (**D**), and SST (**E**) in the equatorial Pacific [red dashed region in (A)] are also shown. The evolution of MSE in the SESP region is rescaled and overlain to illustrate its leading character (blue dashed line). Note that the abscissa in (E) extends through the end of 2021 to illustrate the multiyear persistence of the cooling response.

waves from the western Pacific boundary typically associated with La Niña. The event was also poorly forecast, with major prediction centers such as National Oceanic and Atmospheric Administration–Climate Prediction Center (NOAA-CPC) issuing guidance for ENSO-neutral conditions as late as June 2020. At this time, the emergence of ocean cooling in the eastern Pacific Ocean led some forecasters to favor a La Niña event for late 2020. The results here suggest a potential connection between this emergence of cool conditions in the eastern Pacific Ocean and the climate response to Australian wildfire emissions. The sequence of events connected to this response suggests that in some circumstances, important early influences on tropical Pacific SST can originate from the atmosphere and land surface rather than the equatorial ocean. These, in turn, may represent a predictable component of the coupled system affecting ENSO and serve as a useful complement to the oceanic precursors often used to forecast ENSO. More generally, this analysis also illustrates an interaction between biomass aerosol forcing and ENSO that may become more prevalent under climate change as wildfires are projected to intensify and become more frequent with warming (*19*).

Nonetheless, there are many caveats to consider in our analysis. Foremost are the known biases and uncertainties in CESM2. As discussed, there is a tendency for the model to underestimate aerosol burdens associated with wildfires, and these are highly relevant to simulation of the forced response. The experiments considered here may therefore underestimate the wildfire climate response. There

are also significant uncertainties surrounding the strength and character of aerosol-cloud interactions. Many of these aspects are improved in CESM2 over earlier model versions and other climate models, but considerable uncertainties persist nonetheless (see Materials and Methods). In addition, attributing the contribution of specific climate responses to the simulated tropical Pacific cooling is largely inferred here based on the mutual timing and spatial structure of responses, instead of being directly demonstrated. This attribution is therefore complicated by the presence of multiple potential alternative pathways of influence. The inferences drawn here are supported by early studies examining marine cloud brightening in the SESP region, which also identified La Niña–like responses to cloud deck brightening (*20*, *21*). However, it is also possible that widespread cooling of the southern extratropics (Fig. 3A) can exert an influence on SSTs in the tropical Pacific and the ITCZ (*21*). The interaction between mean state gradients, decadal modes, and ENSO remains an active area of research, and follow-on work is planned to further establish causality in which cloud properties are modified in isolation in the SESP region to estimate the associated tropical response (*22*–*24*).

The relevance of wildfire-aerosol-cloud interactions to both climate seasonal prediction and long-term projection underscores the need to better represent wildfire-climate couplings in models. The future emissions scenarios used in most current climate projections depict a future reduction in total biomass emissions, a highly unlikely outcome in light of current trends (*19*). More realistic scenarios could be achieved, for example, by incorporating biomass emissions as an internal component of the climate system, provided by explicitly depicted wildfire emissions in land models, rather than one that is prescribed or omitted altogether. This may also promote a more realistic simulation of modes of variability and their teleconnections, as strong couplings between internal modes and wildfire, such as for ENSO and fire across the tropics, are known to exist (*25*). Given their broad array of climate influences, wildfires are a key component of the climate system and their representation as an internal coupled climate process is likely to greatly enhance the fidelity of both seasonal climate predictions and long-term projections.

MATERIALS AND METHODS

Community Earth System Model version 2

CESM2 is the most recent coupled Earth system model developed at the National Center for Atmospheric Research (NCAR) in partnership with universities and other research institutions (*13*). The model incorporates a range of novel capabilities and improvements that are directly relevant to the simulation of climate responses to wildfire. These include updated representations of aerosol effects, including consideration of aerosol aging and hydrophilic properties, and their interactions with clouds. An improved treatment of aerosols is provided by the Modal Aerosol Model version 4 (*26*). The Morrison-Gettelman cloud microphysics scheme has also been updated, and mixed-phase ice nucleation is improved to depend on both aerosols and temperature (*26*–*30*). The lifetime of biomass aerosols has also been prolonged from earlier versions to be more realistic. A key additional advance is the inclusion of a unified turbulence scheme that provides a uniform treatment of clouds across cloud types, replacing their more idealized and disjoint representations in earlier model versions (*31*). The CESM2 atmospheric component uses a nominal 1° horizontal resolution with 32 vertical levels but has a relatively coarse stratospheric representation. We use simulations without prognostic chemistry as commonly implemented for climate simulations. Many other advances are also included in CESM2, and recent evaluation of climate models identifies CESM2 as being among the most skillful of available models, based on metrics that compare the model outputs against present-day observations and in reproducing observed modes of variability (*32*, *33*). Specifically, among current global climate models, CESM2 has one of the highest skill scores in reproducing ENSO and the smallest double-ITCZ bias (Fig. 4) (*32*, *33*).

While the representation of smoke and its interactions with clouds and radiation in CESM2 benefits from updates in the aerosol model and advances in the representation of aerosol-cloud interactions, challenges remain. Smoke particles include both the absorbing effects of black carbon and the scattering effects of organic matter (*34*). The observational estimate of direct radiative forcing at the surface from the Australian wildfires was estimated to be -3.0 W m^{-2} from 25°S to 60°S in February 2020, a value consistent with CESM2 simulations (*2*, *4*). However, cloud-aerosol interactions are more difficult to estimate as they broaden the range of radiative effects and depend on the vertical distributions of clouds and aerosols, both of which contain regionally and seasonally dependent biases in models. In CESM2, there is also no plume model and emissions are lofted by grid-scale convection, which is influenced by aerosol radiative heating. The associated response to the fires in the zonal-mean vertical structure of cloud condensation nuclei in CESM2 is shown in fig. S3. While CESM2 provides the opportunity to simulate a broad range of processes relevant to the influence of wildfire emissions on clouds and climate, work remains ongoing to improve the model and reduce associated biases (*4*).

The Seasonal-to-Multiyear Large Ensemble

The control simulations for our experiments are from the Seasonal-to-Multiyear Large Ensemble (SMYLE), which prescribes SSP3-7.0 climatological fire emissions rather than variable emissions (*14*). The SMYLE experiment consists of 2-year-long hindcast simulations that span the period from 1970 to 2019, with seasonal initializations within each year. SMYLE uses CESM2 as its component model and is initialized with data from the Japanese 55-year reanalysis interpolated onto the CESM2 atmospheric grid (*35*). The land initial conditions come from a TRENDY-forced land simulation. The ocean and sea ice initial conditions are based on the forced ocean–sea ice simulations using CESM2, constructed in line with the protocol for version 2 of the Ocean Model Intercomparison Project. SMYLE simulations are forced by smoothed biomass burning emissions, characterized by a mean climatological cycle of the satellite era, which are substituted for the default biomass burning emissions from the Coupled Model Intercomparison Project Phase 6 (CMIP6) due to associated nonlinear model responses (*14*, *36*–*38*). Initial conditions in the ensemble are differentiated by the day of the month chosen at random to begin each simulation. In this work, we focus on predictions beginning in August of 2019, which use the SSP3-7.0 forcing protocols (*36*). Ensemble drift is an intrinsic feature of initialized ensembles and exists in both the SMYLE and AF ensembles. In estimation of the wildfire climate response, ensemble differencing implicitly removes the drift; however, in estimation of raw fields, such as in Fig. 2, it

must be removed explicitly. In Fig. 2, drift in Niño3.4 SST is estimated from the preceding set of August hindcast simulations from 1970 to 2018. Validation of the SMYLE ensemble has been conducted recently (*14*). In this work, additional simulations are performed to augment the SMYLE ensemble. This includes the addition of 10 members to reduce the ensemble standard error. It also involves extending all simulations to 36 months. As the SMYLE ensemble uses climatological fire emissions, we adopt the so-called "only-one" methodology, whereby emissions for the Australian fires are prescribed in a complementary ensemble rather than an "all-but-one" approach, in which the fires are removed and contrasted to a fully forced ensemble.

Global Fire Emissions Database version 4 emissions

Fire emissions for the Australian wildfire season 2019–2020 are prescribed using biomass burning estimates of trace gases and aerosols from the Global Fire Emissions Database version 4 (GFED4) with small fires (*39*). The emissions are created from satellite-measured burned area with small fires added using satellite-measured fire-count information (*40*, *41*). Emissions are conservatively regridded to 0.9° (latitude) × 1.25° (longitude) horizontal resolution to be consistent with CESM2. Species with prescribed emissions include black carbon, POM (calculated as GFED4s organic carbon scaled by 1.4 to account for other trace constituents in organic aerosols), dimethyl sulfide, and sulfur dioxide and sulfate aerosol (2.5% of GFED4s SO_2 is emitted as SO_4, with the remainder as SO_2). Concentrations of ozone and other oxidants are not perturbed as we are isolating the impact of aerosol species. A lumped semivolatile organic gas-phase species is included, which accounts for the creation of secondary organic aerosols by combining various GFED4s species (higher alkanes, higher alkenes, toluene, benzene, xylenes, isoprene, and terpenes). These are then multiplied by a factor of 1.5 (*42*). Our fire emissions are consistent with CMIP6, which uses GFED4s to estimate historical fire emissions (*40*). After July 2020, fire emissions for all ensembles are from SSP3-7.0 (*36*).

Other computations

The field for cloud albedo is generated from the all-sky and clear-sky top-of-atmosphere shortwave fluxes and cloud amount such that the cloudy-sky albedo is estimated from the fractional contribution of cloudy regions to the total grid-cell albedo. The time series shown in Figs. 1, 3, and 4 are generated from daily model output, smoothed with a 10-point Gaussian smoother.

Supplementary Materials

This PDF file includes:

Figs. S1 to S7
References

REFERENCES AND NOTES

1. E. Hirsch, I. Koren, Record-breaking aerosol levels explained by smoke injection into the stratosphere. *Science* **371**, 1269–1274 (2021).
2. S. Khaykin, B. Legras, S. Bucci, P. Sellitto, L. Isaksen, F. Tence, S. Bekki, A. Bourassa, L. Rieger, D. Zawada, J. Jumelet, S. Godin-Beekmann, The 2019/20 Australian wildfires generated a persistent smoke-charged vortex rising up to 35 km altitude. *Commun. Earth Environ.* **1**, 22 (2020).
3. N. G. Loeb, W. Su, N. Bellouin, Y. Ming, Changes in clear-sky shortwave aerosol direct radiative effects since 2002. *J. Geophys. Res. Atmos.* **126**, e2020JD034090 (2021).
4. J. T. Fasullo, N. Rosenbloom, R. R. Buchholz, G. Danabasoglu, D. M. Lawrence, J.-F. Lamarque, Coupled climate responses to recent Australian wildfire and COVID-19 emissions anomalies estimated in CESM2. *Geophys. Res. Lett.* **48**, e2021GL093841 (2021).
5. M. J. McPhaden, A. Santoso, W. Cai, Eds., *El Niño Southern Oscillation in a Changing Climate (Vol. 253)* (John Wiley & Sons, 2020).
6. J. T. Fasullo, B. L. Otto-Bliesner, S. Stevenson, ENSO's changing influence on temperature, precipitation, and wildfire in a warming climate. *Geophys. Res. Lett.* **45**, 9216–9225 (2018).
7. F. S. Pausata, D. Zanchettin, C. Karamperidou, R. Caballero, D. S. Battisti, ITCZ shift and extratropical teleconnections drive ENSO response to volcanic eruptions. *Sci. Adv.* **6**, eaaz5006 (2020).
8. S. McGregor, M. Khodri, N. Maher, M. Ohba, F. S. Pausata, S. Stevenson, The effect of strong volcanic eruptions on ENSO. El Niño Southern Oscillation in a changing climate. *Geophys. Monogr. Ser.*, 267–287 (2020).
9. M. M. Dogar, L. Hermanson, A. Scaife, D. Visioni, M. Zhao, I. Hoteit, H.-F. Graf, M. A. Dogar, M. Almazroui, M. Fujiwara, A review of El Niño Southern Oscillation linkage to strong volcanic eruptions and post-volcanic winter warming. *Earth Syst. Environ.* **7**, 15–42 (2023).
10. J. T. Fasullo, B. L. Otto-Bliesner, S. Stevenson, The influence of volcanic aerosol meridional structure on monsoon responses over the last millennium. *Geophys. Res. Lett.* **46**, 12350–12359 (2019).
11. T. Schneider, T. Bischoff, G. H. Haug, Migrations and dynamics of the intertropical convergence zone. *Nature* **513**, 45–53 (2014).
12. B. Ward, F. S. Pausata, N. Maher, The sensitivity of the El Niño–Southern Oscillation to volcanic aerosol spatial distribution in the MPI grand ensemble. *Earth Syst. Dynam.* **12**, 975–996 (2021).
13. G. Danabasoglu, J.-F. Lamarque, J. Bacmeister, D. Bailey, A. DuVivier, J. Edwards, L. Emmons, J. Fasullo, R. Garcia, A. Gettelman, C. Hannay, M. M. Holland, W. G. Large, P. H. Lauritzen, D. M. Lawrence, J. T. M. Lenaerts, K. Lindsay, W. H. Lipscomb, M. J. Mills, R. Neale, K. W. Oleson, B. Otto-Bliesner, A. S. Phillips, W. Sacks, S. Tilmes, L. van Kampenhout, M. Vertenstein, A. Bertini, J. Dennis, C. Deser, C. Fischer, B. Fox-Kemper, J. E. Kay, D. Kinnison, P. J. Kushner, V. E. Larson, M. C. Long, S. Mickelson, J. K. Moore, E. Nienhouse, L. Polvani, P. J. Rasch, W. G. Strand, The community earth system model version 2 (CESM2). *J. Adv. Model. Earth Syst.* **12**, e2019MS001916 (2020).
14. S. G. Yeager, N. Rosenbloom, A. A. Glanville, X. Wu, I. Simpson, H. Li, M. J. Molina, K. Krumhardt, S. Mogen, K. Lindsay, D. Lombardozzi, W. Wieder, W. M. Kim, J. H. Richter, M. Long, G. Danabasoglu, D. Bailey, M. Holland, N. Lovenduski, W. G. Strand, T. King, The Seasonal-to-Multiyear Large Ensemble (SMYLE) Prediction System using the Community Earth System Model version 2. *Geosci. Model Dev.* **15**, 6451–6493 (2022).
15. J. Russell-Smith, C. P. Yates, P. J. Whitehead, R. Smith, R. Craig, G. E. Allan, R. Thackway, I. Frakes, S. Cridland, M. C. P. Meyer, A. M. Gill, Bushfires 'down under': Patterns and implications of contemporary Australian landscape burning. *Int. J. Wildland Fire* **16**, 361–377 (2007).
16. X. Jiang, E. Maloney, H. Su, Large-scale controls of propagation of the Madden-Julian oscillation. *NPJ Clim. Atmos. Sci.* **3**, 29 (2020).
17. X. Li, Z.-Z. Hu, Y.-H. Tseng, Y. Liu, P. Liang, A historical perspective of the La Niña event in 2020/2021. *J. Geophys. Res. Atmos.* **127**, e2021JD035546 (2022).
18. F. S. R. Pausata, Y. Zhao, D. Zanchettin, R. Caballero, D. S. Battisti, Revisiting the mechanisms of ENSO response to tropical volcanic eruptions. *Geophys. Res. Lett.* **50**, e2022GL102183 (2023).
19. M. W. Jones, A. Smith, R. Betts, J. G. Canadell, I. C. Prentice, C. Le Quéré, Climate change increases the risk of wildfires. *ScienceBrief Rev.* **116**, 117 (2020).
20. A. Jones, J. Haywood, O. Boucher, Climate impacts of geoengineering marine stratocumulus clouds. *J. Geophys. Res. Atmos.* **114**, D10 (2009).
21. S. Hill, Y. Ming, Nonlinear climate response to regional brightening of tropical marine stratocumulus. *Geophys. Res. Lett.* **39**, L15707 (2012).
22. Y. Dong, K. C. Armour, D. S. Battisti, E. Blanchard-Wrigglesworth, Two-way teleconnections between the Southern Ocean and the tropical Pacific via a dynamic feedback. *J. Climate* **35**, 2667–2682 (2022).
23. J. Zhu, A. Kumar, B. Huang, M. A. Balmaseda, Z. Z. Hu, L. Marx, J. L. Kinter III, The role of off-equatorial surface temperature anomalies in the 2014 El Niño prediction. *Sci. Rep.* **6**, 19677 (2016).
24. Z.-Z. Hu, A. Kumar, B. Huang, J. Zhu, M. L'Heureux, M. J. McPhaden, J.-Y. Yu, The interdecadal shift of ENSO properties in 1999/2000: A review. *J. Climate* **33**, 4441–4462 (2020).
25. Y. Chen, D. C. Morton, N. Andela, G. R. van der Werf, L. Giglio, J. T. Randerson, A pan-tropical cascade of fire driven by El Niño/Southern Oscillation. *Nat. Clim. Chang.* **7**, 906–911 (2017).
26. X. Liu, P. L. Ma, H. Wang, S. Tilmes, B. Singh, R. C. Easter, S. J. Ghan, P. J. Rasch, Description and evaluation of a new four-mode version of the Modal Aerosol Module (MAM4) within version 5.3 of the Community Atmosphere Model. *Geosci. Model Dev.* **9**, 505–522 (2016).
27. A. Gettelman, H. Morrison, Advanced two-moment bulk microphysics for global models. Part I: Off-line tests and comparison with other schemes. *J. Climate* **28**, 1268–1287 (2015).

28. C. Hoose, J. E. Kristjánsson, J.-P. Chen, A. A. Hazra, A Classical-theory-based parameterization of heterogeneous ice nucleation by mineral dust, soot, and biological particles in a global climate model. *J. Atmos. Sci.* **67**, 2483–2503 (2010).
29. Y. Wang, X. Liu, C. Hoose, B. Wang, Different contact angle distributions for heterogeneous ice nucleation in the community atmospheric model version 5. *Atmos. Chem. Phys.* **14**, 10411–10430 (2014).
30. X. Shi, X. Liu, K. Zhang, Effects of preexisting ice crystals on cirrus clouds and comparison between different ice nucleation parameterizations with the Community Atmosphere Model (CAM5). *Atmos. Chem. Phys.* **15**, 1503–1520 (2015).
31. P. A. Bogenschutz, A. Gettelman, H. Morrison, V. E. Larson, C. Craig, D. P. Schanen, Higher-order turbulence closure and its impact on climate simulations in the community atmosphere model. *J. Climate* **26**, 9655–9676 (2013).
32. J. T. Fasullo, Evaluating simulated climate patterns from the CMIP archives using satellite and reanalysis datasets using the Climate Model Assessment Tool (CMATv1). *Geosci. Model Dev.* **13**, 3627–3642 (2020).
33. J. T. Fasullo, A. S. Phillips, C. Deser, Evaluation of leading modes of climate variability in the CMIP archives. *J. Climate* **33**, 5527–5545 (2020).
34. I. N. Sokolik, A. J. Soja, P. J. DeMott, D. Winker, Progress and challenges in quantifying wildfire smoke emissions, their properties, transport, and atmospheric impacts. *J. Geophys. Res. Atmos.* **124**, 13005–13025 (2019).
35. S. Kobayashi, Y. Ota, Y. Harada, A. Ebita, M. Moriya, H. Onoda, K. Onogi, H. Kamahori, C. Kobayashi, H. Endo, K. Miyaoka, K. Takahashi, The JRA-55 reanalysis: General specifications and basic characteristics. *J. Meteorol. Soc. Japan* **93**, 5–48 (2015).
36. B. Eyring, S. Bony, G. A. Meehl, C. A. Senior, B. Stevens, R. J. Stouffer, K. E. Taylor, Overview of the Coupled Model Intercomparison Project Phase 6 (CMIP6) experimental design and organization. *Geosci. Model Dev.* **9**, 1937–1958 (2016).
37. M. J. E. van Marle, S. Kloster, B. I. Magi, J. R. Marlon, A.-L. Daniau, R. D. Field, A. Arneth, M. Forrest, S. Hantson, N. M. Kehrwald, W. Knorr, G. Lasslop, F. Li, S. Mangeon, C. Yue, J. W. Kaiser, G. R. van der Werf, Historic global biomass burning emissions for CMIP6 (BB4CMIP) based on merging satellite observations with proxies and fire models (1750–2015). *Geosci. Model Dev.* **10**, 3329–3357 (2017).
38. J. T. Fasullo, J.-F. Lamarque, C. Hannay, N. Rosenbloom, S. Tilmes, P. DeRepentigny, A. Jahn, C. Deser, Spurious late historical-era warming in CESM2 driven by prescribed biomass burning emissions. *Geophys. Res. Lett.* **49**, e2021GL097420 (2022).
39. G. R. van der Werf, J. T. Randerson, L. Giglio, T. T. van Leeuwen, Y. Chen, B. M. Rogers, M. Mu, M. J. van Marle, D. C. Morton, G. J. Collatz, R. J. Yokelson, P. S. Kasibhatla, Global fire emissions estimates during 1997–2016. *Earth Syst. Sci. Data* **9**, 697–720 (2017).
40. L. Giglio, J. T. Randerson, G. R. van der Werf, Analysis of daily, monthly, and annual burned area using the fourth-generation global fire emissions database (GFED4). *J. Geophys. Res. Biogeo.* **118**, 317–328 (2013).
41. J. T. Randerson, Y. Chen, G. R. van der Werf, B. M. Rogers, D. C. Morton, Global burned area and biomass burning emissions from small fires. *J. Geophys. Res.* **117**, G04012 (2012).
42. S. Tilmes, A. Hodzic, L. K. Emmons, M. J. Mills, A. Gettelman, D. E. Kinnison, M. Park, J.-F. Lamarque, F. Vitt, M. Shrivastava, P. Campuzano-Jost, J. L. Jimenez, X. Liu, Climate forcing and trends of organic aerosols in the Community Earth System Model (CESM2). *J. Adv. Model. Earth Syst.* **11**, 4323–4351 (2019).
43. R. C. Levy, S. Mattoo, L. A. Munchak, L. A. Remer, A. M. Sayer, F. Patadia, N. C. Hsu, The collection 6 MODIS aerosol products over land and ocean. *Atmos. Meas. Tech.* **6**, 2989–3034 (2013).
44. A. M. Sayer, L. A. Munchak, N. C. Hsu, R. C. Levy, C. Bettenhausen, M.-J. Jeong, MODIS collection 6 aerosol products: Comparison between Aqua's e-Deep Blue, Dark Target, and "merged" data sets, and usage recommendations. *J. Geophys. Res. Atmos.* **119**, 13,965–13,989 (2014).

Acknowledgments

Funding: The efforts of J.T.F. in this work were supported by NASA awards 80NSSC17K0565 and 80NSSC22K0046 and by the Regional and Global Model Analysis (RGMA) component of the Earth and Environmental System Modeling Program of the U.S. Department of Energy's Office of Biological and Environmental Research (BER) via National Science Foundation IA 1947282. N.R. is also supported by the RGMA via National Science Foundation IA 1947282. **Author contributions:** Conceptualization: J.T.F., N.R., and R.B. Methodology: J.T.F., N.R., and R.B. Investigation: J.T.F. Visualization: J.T.F. Supervision: J.T.F., N.R., and R.B. Writing—original draft: J.T.F. Writing—review and editing: J.T.F., N.R., and R.B. **Competing interests:** J.T.F. is a member of the ATOC department at the University of Colorado. The authors declare that they have no competing interests. **Data and materials availability:** The SMYLE project webpage at https://cesm.ucar.edu/working-groups/earth-system/simulations/smyle includes pointers to SMYLE data and references, contact information, and instructions for how to replicate the experiment. Output data from SMYLE hindcast simulations as well as from the historical reconstructions used for initialization (the SMYLE FOSI and forced CLM5 runs) are available from NCAR's Climate Data Gateway at https://doi.org/10.26024/pwma-re41. The additional experiments described above are made available at the Geoscience Data Exchange at https://gdex.ucar.edu under DASH-354: CESM2 Initialized 2019/20 Australian Wildfire Simulations. All data needed to evaluate the conclusions in the paper are present in the paper and/or the Supplementary Materials.

Submitted 3 December 2022
Accepted 6 April 2023
Published 10 May 2023
10.1126/sciadv.adg1213